A BCS microwave imaging algorithm for object detection and shape reconstruction tested with experimental data

N. Zilberstein, J. A. Maya, and A. Altieri

An approach based on the Green function and the Born approximation is used for impulsive radio ultra-wideband (UWB) microwave imaging, in which a permittivity map of the illuminated scenario is estimated using the scattered fields measured at several positions. Two algorithms are applied to this model and compared: the first one solves the inversion problem using a linear operator. The second one is based on the Bayesian compressive sensing (BCS) technique, where the sparseness of the contrast function is introduced as *a priori* knowledge in order to improve the inverse mapping. In order to compare both methods, measurements in real scenarios are taken using an UWB radar prototype. The results with real measurements illustrate that, for the considered scenarios, the BCS imaging algorithm has a better performance in terms of range and cross-range resolution allowing object detection and shape reconstruction, with a reduced computational burden, and fewer space and frequency measurements, as compared to the linear operator.

Introduction: Microwave imaging techniques using UWB signals have been widely studied in recent years due to the various applications in different fields, such as breast cancer detection [1], SAR image classification [2], ground penetrating radars systems [3], and material sample characterization [4]. However, inverse microwave imaging problems are intrinsically challenging due to their non-linear nature and ill-posedness [5], and algorithms are in continuously developing. Different approaches have been used for building qualitative and quantitative microwave images. In the former, the objective is to detect changes in the permittivity map without trying to obtain the true value of permittivity of the target. For these cases, linear problems can be formulated and solved using several techniques as diffraction summation and F-K migration. Furthermore, linearization methods of the non-linear equations resulting from the scattering theory using the Born approximation and the Green function are well-established first principles models [6].

In the case of quantitative microwave images, it is expected to estimate the true value of the permittivity map and typically, the non-linear problem has to be solved. For example, this is the case of the contrast-source formulation, which is based on an iterative method. In this paper we are interested in detecting the location and shape of metallic and dielectric objects, which finds several applications [7–9]. Therefore, we follow the first approach to estimate a qualitative microwave image using a model based on the Born approximation (BA).

Additionally, to improve the conditioning of the problem, the use of schemes which take advantage of a priori information helps to increase the robustness of the solutions and the overall performance of the estimators. Also, typical inversion schemes require the acquisition and storage of a large number of measurements over the region of interest. This is costly and involved, so the development of schemes which achieve a good performance with a small set of measurements is of interest in most practical scenarios. In this context, compressive sensing (CS) techniques have been applied to the inverse problem at hand where the signal to be estimated is sparse in some basis. An interesting approach is the Bayesian compressive sensing (BCS) framework [10, 11], which has been applied to inverse problems showing promising results. However, in most works in the literature, its performance is evaluated using synthetic data in 2-D scenarios [12, 13].

In this work, we employ a BCS algorithm for object detection and shape reconstruction. We evaluate its performance in 3-D scenarios with experimental data, where conditions are more adverse due to non-linearity, noise and jitter in the electronic devices, interference from sources outside of the experiment, and non-desired echoes produced by scatterers other than the targets. The physical model that we use is strictly valid for scenarios

with cylindrical symmetry. Despite that in practical scenarios this assumption is clearly not satisfied, we show that the model allows to obtain good performance tomographic images of the permittivity map. We compare the performance of the BCS algorithm with a reconstruction technique, frequently used in the literature [9, 14], which uses the adjoint operator (AO) that maps the contrast function into the measured scatter fields (under the Born approximation). Different targets are tested in order to show the capacity of the BCS imaging algorithm to detect the presence of the object and estimate its geometric shape.

This work is organized as follows. First we present the model and the AO algorithm. Second, we apply the BCS algorithm to obtain the microwave image. Then, we present the results, and finally, draw the main conclusions.

Problem Formulation: Let us consider the scenario sketched in Fig. 1, where a single-input single-output configuration is used to obtain a tomographic image (over the $xz-$plane for a fixed y_0) of the observation domain $D_{obs} = \{\boldsymbol{r} = (x,z) : z < 0\}$. Assume that the transmitting and receiving antennas are located at N_a positions $\boldsymbol{r}_{rn} = (x_{rn}, z_0)$ and $\boldsymbol{r}_{tn} = (x_{tn}, z_0)$, respectively, where the center position of the Tx-Rx system $x_{cn} = \frac{x_{tn}+x_{rn}}{2}$ is moved in the interval $[x_{min}, x_{max}]$ and $z_0 = 0$. We consider the common offset acquisition method, where the distance between the Tx and Rx antennas is fixed. The system has -10 dB bandwidth $B = [f_{min}, f_{max}]$, which is divided in M_f bins. We consider scenarios without interface, although it is straightforward to extend the results to scenarios with multiple layers given that we only have to recompute the Green function [15]. The observation domain is illuminated by the
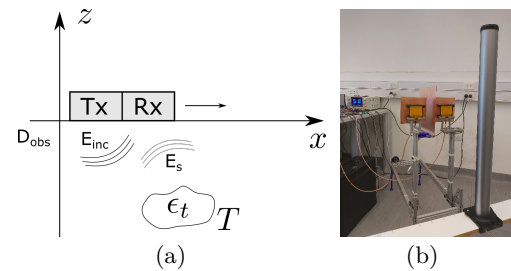

Fig. 1 *(a) Schematic representation of the setup, and (b) experimental setup for Scenario 1.*

incident electric field $\boldsymbol{E}_{inc}$, generated by the transmitting antenna Tx. The interaction of $\boldsymbol{E}_{inc}$ with the scatterers produces the scattered electric field $\boldsymbol{E}_s$. The total electric field is $\boldsymbol{E}_{tot} = \boldsymbol{E}_{inc} + \boldsymbol{E}_s$. Under the assumption that $\boldsymbol{E}_{inc}$ has a linear polarization in the y component, i.e, $\boldsymbol{E}_{inc} = E_{inc} \, \hat{\boldsymbol{y}}$, and that the observation domain has cylindrical symmetry (with an arbitrary section) also through the y component, the Green function, which is the impulse response of the system, is a scalar function (instead of a tensor). In fact, this is the case if we consider as an excitation a 3-D line source directed in the y direction. Under these hypotheses and using the BA for *weak* scatterers [5], where the total electric field is approximated by the incident field, the scattered electric field measured at $\boldsymbol{r}_{rn}$ for a fixed wave number k can be written as

$$E_s(\boldsymbol{r}_{rn}, k) = k^2 \int_{D_{obs}} \Delta \epsilon_t(\boldsymbol{r}) E_{inc}(\boldsymbol{r}, \boldsymbol{r}_{tn}, k) g(\boldsymbol{r}_{rn}, \boldsymbol{r}, k) d\boldsymbol{r}, \quad (1)$$

where $\boldsymbol{r}$ represents the different positions of the scenario under investigation, $E_{inc}(\boldsymbol{r}, \boldsymbol{r}_{tn}, k) = \imath \eta_0 k P(k) g(\boldsymbol{r}, \boldsymbol{r}_{tn}, k)$ is the incident field produced by the source at position $\boldsymbol{r}_{tn}$ and measured at $\boldsymbol{r}$, η_0 is the intrinsic impedance of free space ($\approx 377\Omega$), and $P(k)$ is the Fourier transform of the pulse transmitted by the Tx. The wave number k is related to the frequency f in Hertz through the equation $k = 2\pi f/c$, where c is the speed of light in free space. For the homogeneous case under consideration (without considering the target), $g(\boldsymbol{r}_{rn}, \boldsymbol{r}, k) = \frac{\imath}{4} H_0^{(2)}(k\|\boldsymbol{r} - \boldsymbol{r}_{rn}\|)$ is the scalar Green function, where $H_0^{(2)}$ is the Hankel function of second kind and order 0[1]. Finally, $\Delta \epsilon_t = \epsilon_{rt}(\boldsymbol{r}) - \epsilon_{rb}$ is the contrast function, where in this case the background relative permittivity is $\epsilon_{rb} = 1$ and ϵ_{rt}

---

[1] The time harmonic convention $\exp(\imath 2\pi f t)$ is used here.

is the relative permittivity of the target. Note that $\Delta\epsilon_t$ is non-zero only in the target position.

Equation (1) can be expressed by a linear operator applied to the contrast function. Then the microwave image can be obtained using its adjoint operator applied to the measured scattered electric field [14, 15] as:

$$\hat{\Delta}\epsilon_r(\boldsymbol{r}) = -\imath\eta_0 \int_{k_{min}}^{k_{max}} dk P(k)k^3 \int_{x_{min}}^{x_{max}} dx_{cn}\, g^*(\boldsymbol{r}_{rn}, \boldsymbol{r}, k)$$
$$\times g^*(\boldsymbol{r}_{rn}, \boldsymbol{r}, k) E_s(\boldsymbol{r}_{rn}, k), \quad (2)$$

where the limits of the outer integral are $k_{min/max} = \frac{2\pi}{c} f_{min/max}$, and $*$ means complex conjugate.

Discrete Model for BCS In order to obtain a solution for (1), the domain is discretized using a basis of indicator functions, i.e.,

$$\theta^n(\mathbf{r}) = \begin{cases} 1 \text{ si } \mathbf{r} \in D^n, \\ 0 \text{ si } \mathbf{r} \notin D^n, \end{cases} \quad n = 1, ..., N \quad (3)$$

where D_{obs} is divided in N pixels and D^n is the n-th pixel. Then, the contrast function is approximated by a piecewise 2-D constant function

$$\Delta\epsilon_r(\mathbf{r}) \simeq \sum_{n=1}^{N} w_n\, \theta^n(\mathbf{r}), \quad (4)$$

and we obtain a matrix formulation of the problem,

$$\mathbf{E_s} = \mathbb{G}\mathbf{w},$$

where the elements of $\mathbf{w} \in \mathbb{C}^N$, $\mathbb{G} \in \mathbb{C}^{M_f N_a \times N}$ and $\mathbf{E_s} \in \mathbb{C}^{M_f N_a}$ are, respectively, $(\mathbf{w})_j = w_j$, $(\mathbf{E_s})_l = E_s(\boldsymbol{r}_{rj}, k_q)$ and

$$(\mathbb{G})_{l,n} = \imath\eta_0 k_q^3 P(k_q) \int_{D^n} g(\mathbf{r}, \mathbf{r}_{tj}, k_q) g(\mathbf{r}_{rj}, \mathbf{r}, k_q)\theta^n(\mathbf{r})d\mathbf{r}, \quad (5)$$

with $l = q + (j-1)M_f$, $1 \le j \le N_a$, $1 \le q \le M_f$, $1 \le n \le N$. This means that for the position of each Tx-Rx pair there are M_f wave number (frequency) samples, where k_q is the wave number a the center of the $q-$th bin.

Bayesian Compressive Sensing: We consider the case where the measurements of the electric field are noisy, and the noise is zero-mean white normally distributed with variance σ^2, i.e,

$$\mathbf{E_s} = \mathbb{G}\mathbf{w} + \mathbf{N}, \ \ \mathbf{N} \sim \mathcal{N}(\mathbf{0}, \sigma^2\mathbf{I}), \quad (6)$$

where $\mathbf{I}$ is the identity matrix of size $M_f N_a \times M_f N_a$. This equation defines a linear problem for estimating $\mathbf{w}$ from $\mathbf{E_s}$. In scenarios where the size of the target is much smaller than the observation domain[2], the contrast function defined in the previous section is a *sparse* signal, meaning that only a few components of $\mathbf{w}$ are different from zero. Then, a compressive sensing approach can be used. In particular, we used the BCS approach, which is a framework where a compressive sampling approach is used. In other words, the measurements are obtained as a linear combination of the projection of the signal $\mathbb{G}\mathbf{w}$ onto a random basis. We define the sensing matrix $\boldsymbol{\Psi} \in \{0, 1\}^{N_s \times M_f N_a}$ as a selection matrix, i.e. a matrix with orthogonal rows and a unique non-zero component in each row with value 1, which selects N_s components of $\mathbf{E_s}$:

$$\mathbf{t} = \boldsymbol{\Psi}\mathbf{E_s} = \boldsymbol{\Phi}\mathbf{w} + \mathbf{N}, \ \ \boldsymbol{\Phi} = \boldsymbol{\Psi}\mathbb{G}. \quad (7)$$

An advantage of using a probabilistic framework is that it is not required to satisfy the restricted isometry property (RIP) on the $\boldsymbol{\Phi}$ matrix. The image problem using BCS is formulated as follows: given the measurements $\mathbf{t}$, obtain

$$\hat{\mathbf{w}} = \arg\max_{\mathbf{w}} p(\mathbf{w}|\mathbf{t}) \quad (8)$$

where $p(\mathbf{w}|\mathbf{t})$ is the *a posteriori* density function. Following [16], a closed-form solution to this problem can be obtained if $p(\mathbf{w}|\mathbf{t}) = \int p(\mathbf{w}|\mathbf{t}, \boldsymbol{\alpha}, \sigma^2)p(\boldsymbol{\alpha}, \sigma^2|\mathbf{t})d\boldsymbol{\alpha}d\sigma^2 \approx p(\mathbf{w}|\mathbf{t}, \boldsymbol{\alpha}_{\text{MP}}, \sigma^2_{\text{MP}}) = \mathcal{N}(\boldsymbol{\mu}, \boldsymbol{\Sigma})$, where $\boldsymbol{\mu} = \sigma^{-2}\boldsymbol{\Sigma}\boldsymbol{\Phi}^T\mathbf{t}$, $\boldsymbol{\Sigma} = (\sigma^{-2}\boldsymbol{\Phi}^T\boldsymbol{\Phi} + \mathbf{A})^{-1}$, and $\mathbf{A} = \text{diag}(\alpha_1, ..., \alpha_N)$ is a diagonal matrix. Thus, the problem (8) has solution $\hat{\mathbf{w}} = \boldsymbol{\mu}$, and the so-called hyper-parameters $\boldsymbol{\alpha}_{\text{MP}}$ and σ^2_{MP} are computed as in [16], and the image is constructed using (4).

---

[2] In other scenarios one typically can find an adequate basis to explain $\mathbf{w}$ through few coefficients.

Results: In order to evaluate the advantages of the BCS algorithm compared to the direct inversion technique in Eq. (2), we measured different targets in air: a metallic cylinder and a tank with water. We use an impulsive UWB radar to acquire the time-domain measurements of the electric field at N_a positions in the x-direction. The antennas are only moved in a linear motion in front of the target to mimic scenarios in which the target is embedded in a material which is only accessible from one side.

The scattered electric field is needed as an input to the algorithms (Eqs. (2) and (7)). In order to obtain it, the incident electric field E_{inc} is measured without the target and then it is subtracted from each measurement. As we need the signal in the frequency domain, we use the FFT to transform each time-trace.

The size of the pixels D^n is $2\,\text{cm} \times 1\,\text{cm}$. This value was selected as a trade-off between computation time of the algorithm and good resolution of the reconstructed targets. The observation domain for the first experiment is $x_{max} - x_{min} = 2.2\,\text{m}$, with measurement steps of 5 cm for the position of Tx and Rx resulting $N_a = 41$. For the others scenarios, the length of the domain is $x_{max} - x_{min} = 1.1\,\text{m}$, with the same step and $N_a = 21$.

A custom test-bed hardware was built using off-the-shelf components. A field programmable gate array (FPGA) is used to generate a train of narrow pulses which is then upconverted to the carrier frequency $f_c = 1.9\text{GHz}$, amplified and then transmitted. The receiver architecture is composed of a low-noise amplifier, a bandpass filter and a single-stage zero-frequency I/Q demodulator. After the conversion to baseband, the I and Q signals are amplified via a high linearity differential driver amplifier which feeds a high speed dual channel analog-to-digital converter (ADC), operating with a sampling frequency $f_s = 1.8\text{GS/s}$. A real-time sampling strategy was used for this prototype, mainly for reasons of availability, but an equivalent-time sampling strategy could also be used to achieve a substantial reduction in hardware costs. The ADC is controlled by the same FPGA which is used to generate the pulses, which allows for an easy synchronization between the transmitted pulses and the receiver. The FPGA will generate a pulse train composed of $N_p = 91$ pulses, with a pulse period of $T_s = 100\text{ns}$. At the receiver, the scattered pulses will be coherently combined to obtain an increase in the signal to interference and noise ratio (SINR) of the received signal.

The antennas are printed elliptical monopole antennas [17], which have the advantage of being low-cost, simple to design, compact and planar. One of their disadvantages is that their radiation pattern is not very directional. In order to improve their directionality, a square reflector of side 160mm (the wavelength at the central frequency of 1.9GHz) was placed behind each antenna at a distance of 39mm (a quarter wavelength at the antenna central frequency). The two antennas were placed side-by-side, and, in order to reduce their mutual coupling, a conductive reflector was placed between the two. The horizontal separation between the antennas was chosen to be 200mm. A single antenna with its reflector has an azimuth 3dB beam width of 80°, and an elevation beam width of approximately 110°. The antennas are linearly polarized in the vertical direction and their boresight gain is approximately 10dB. The antenna setup can be seen in Fig. 1(a).

The resolution of the image is limited by the hardware (bandwidth), the antenna characteristics (central frequency, fundamentally), and the setup configuration, and can be analyzed through the point spread function (PSF). The resolution in the x and z direction are $\delta x \approx \frac{c}{f_c} = 15.8\,\text{cm}$ and $\delta z = \frac{c}{B} = 30\,\text{cm}$, respectively.

Scenario 1: Metallic cylinder. The first experiment was done using a metallic cylinder with a diameter of 6cm and a height of 70cm as a target. Its position in the (x, z) plane (using the coordinate system of Fig. 1(a)) was $\boldsymbol{r}_t = (1.1\,\text{m}, -42.7\,\text{cm})$. The experimental setup is shown in Fig. 1(b). For the BCS algorithm, a random sampling both in space and frequency was used: 10 pairs of Tx/Rx positions and 10 frequency bins were selected from a total number of 41 positions and 100 frequency bins. So, for BCS only a 25% of spatial measurements were used and 10% of the frequencies. The results obtained using both AO and BCS algorithms are shown in Figs. 2(a) and 2(b) respectively. In both cases, the black circle represents the true target. The scale is normalized with respect to the absolute maximum. The position and size of the cylinder

are successfully estimated using both algorithms. Although the weak scattering hypothesis in the BA fails due to a high contrast target, the model is still valid for estimating its geometry. This can be explained by noting that the support of the contrast source that generates the scattered electric field is the same for both the incident electric field and the total electric field. Note also that the BCS algorithm achieves much better resolution than the OA algorithm, especially in the range (z) direction, improving the resolution predicted by the PSF analysis. Additionally, this experiment allows us to validate the use of the 3-D model with cylindrical symmetry in this scenario, in spite of the extension of the metallic cylinder finite and the transmitting antenna is not a line source but a linear polarized finite-size directional antenna, with the target centered respect to it in the y direction.
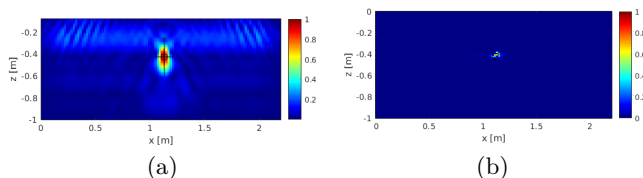

(a)

(b)

Fig. 2. Scenario 1: metallic cylinder. (a) AO and (b) BCS.

Scenario 2: water tank. In this case, the target was a plastic tank filled with water ($\epsilon_{rt} \approx 80$), with the shape of a rectangular prism; its width, height and depth are $22.8\,\mathrm{cm} \times 32.5\,\mathrm{cm} \times 3.2\,\mathrm{cm}$, respectively. The position was $r = (0.55\,\mathrm{m}, -42.7\,\mathrm{cm})$. In Fig. 3(a) the reconstruction with the AO algorithm is shown while Fig. 3(b) corresponds to the BCS algorithm. For BCS, 10 Tx/Rx (50%) were used and the number of frequencies bins is 10 (10% of the total).
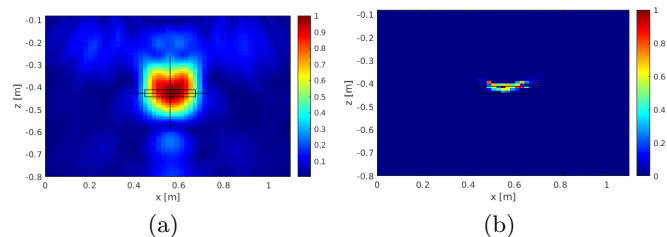

(a)

(b)

Fig. 3. Scenario 2: water tank. (a) AO and (b) BCS

In this case, the target has a rectangular shape whose perimeter is shown in the figure with a black line. Similar to the previous experiment, the advantage that BCS presents with respect to the AO is the increased spatial resolution, allowing in this case to estimate the frontal shape of the target with more precision.

Scenario 3: rotated water tank. In this scenario the same tank of Scenario 2 was used, but rotated approximately $10°$ with respect to the antennas, as shown in Fig. 4(a). The position was $r = (0.55\,\mathrm{m}, -42.7\,\mathrm{cm})$. For the BCS algorithm, 15 random positions for Tx/Rx and 50 frequencies bins were taken.
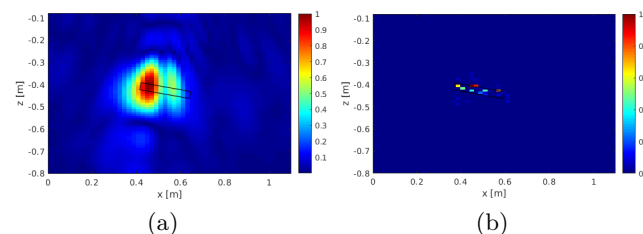

(a)

(b)

Fig. 4. Scenario 3: rotated water tank. (a) AO and (b) BCS.

From Fig. 4(a) it is clear that the AO algorithm detects the position but does not manage to estimate accurately neither the rotation nor the shape. On the other hand, the performance of the BCS algorithm is better, as it estimates well the position, allows to see the rotation of the target and permits to reconstruct, at least partially, the front of its shape (see Fig. 4(b)).

Conclusions: In this paper we evaluated two microwave imaging algorithms with experimental data obtained with a impulsive UWB radar test-bed in different scenarios. From the experiments we draw the following conclusions: i) For point targets, like Scenario 1, or moderately complex scenarios such as the rotated water tank of Scenario 3, both algorithms detect the position of the targets but BCS is able to detect the shape of the target better. ii) The number of measurements when using BCS can be substantially reduced, but not with the adjoint operator. This allows to reduce the complexity of measurement system, the time taken to perform the measurements, and the processing time of the algorithm. iii) The spatial resolution is improved with the BCS algorithm given that better discrimination is obtained. iv) The 2-D physical model is a good model for a practical 3-D scenarios when a tomographic microwave image is required. Although in real scenarios as the examined here the hypothesis of cylindrical symmetry of the target does not hold, the algorithms perform well as they can detect the position and shape of the targets.

Nicolás Zilberstein (*Universidad de Buenos Aires, Facultad de Ingeniería, Buenos Aires, Argentina.*), Juan Augusto Maya, and Andrés Altieri (*CSC-CONICET and Universidad de Buenos Aires, Facultad de Ingeniería, Buenos Aires, Argentina.*)

E-mail: jmaya@fi.uba.ar

References

1 N. Z. Naghsh, A. Ghorbani, and H. Amindavar. Compressive sensing for microwave breast cancer imaging. *IET Sig. Proc.*, 12(2):242–246, Sept. 2017. IET Digital Library.

2 S. Xia, Ze Yu, and JinDong Yu. Adaptive convolutional network for SAR image classification. *The Journal of Engineering*, 2019(20):6868–6872, July 2019. IET Digital Library.

3 X. Xu, et al. Integrated synchronous data acquisition subsystem for high-speed GPR system. *IET Circuits, Devices and Systems*, 13(7):1049–1055, June 2019. IET Digital Library.

4 H. Mextorf, et al. New uwb free-space method for the classification and characterization of dielectric objects. In *2011 IEEE Int. Conf. on Ultra-Wideband (ICUWB)*, pages 380–384, Sep. 2011.

5 W. Chew. *Waves and fields in inhomogeneous media.* IEEE press, 1995.

6 G. Leone and F. Soldovieri. Analysis of the distorted born approximation for subsurface reconstruction: truncation and uncertainties effects. *IEEE Trans. Geos. Rem. Sens.*, 41(1):66–74, Jan. 2003.

7 S. Tantong, et al. Near-Field Microwave Imaging Techniques for Object Detection and Shape Reconstruction. In *2007 IEEE Reg. 5 Tech. Conf.*, pp 299–302, April 2007.

8 N. Irishina, et al. Detecting and imaging dielectric objects from real data: A shape-based approach. *Mathematical and Computer Modelling*, 50(5):743–749, September 2009.

9 O. Dorn, E.L. Miller, and C.M. Rappaport. A shape reconstruction method for electromagnetic tomography using adjoint fields and level sets. *Inverse problems*, 16(5):1119, 2000.

10 S. Ji, Y. Xue, and L. Carin. Bayesian compressive sensing. *IEEE Trans. on Sig. Proc.*, 56(6):2346–2356, June 2008.

11 M. Tipping. Sparse bayesian learning and the relevance vector machine. *J. Mach. Learn. Res.*, 1:211–244, Sept. 2001.

12 A. E. Fouda and F. L. Teixeira. Ultra-wideband microwave imaging of breast cancer tumors via bayesian inverse scattering. *Journal of Applied Physics*, 115(6):064701, 2014.

13 L. Poli et al. Microwave imaging within the first-order born approximation by means of the contrast-field bayesian compressive sensing. *IEEE Trans. Ant. Prop.*, 60(6):2865–2879, Jun. 2012.

14 Y. L. Liu, L. L. Li, and F. Li. Imaging of two-dimensional targets buried in a lossy earth with unknown characteristics from multifrequency and multi-monostatic data. *IET Microwaves, Antennas Propagation*, 4(10):1647–1653, October 2010.

15 W. Zhang. Two-dimensional microwave tomographic algorithm for radar imaging through multi layered media. *Progress In Electr. Research*, 144:261–270, 2014.

16 M.E. Tipping, and A.C. Faul. Fast marginal likelihood maximisation for sparse bayesian models. In *AISTATS*, 2003.

17 J. Liang, C.C. Chiau, X. Chen, and C.G. Parini. Study of a printed circular disc monopole antenna for UWB systems. *IEEE Trans. on Ant. and Prop.*, 53(11):3500–3504, Nov. 2005.